*J. Fluid Mech.* (1999), *vol.* 383, *pp.* 229–247. Printed in the United Kingdom



# An experimental study of recirculating flow through fluid–sediment interfaces

By A. KHALILI[1], A. J. BASU[2], U. PIETRZYK[3] AND M. RAFFEL[4]

[1]Max Planck Institute for Marine Microbiology, 28359 Bremen, Germany
[2]Jawaharlal Nehru Centre for Advanced Scientific Research, Bangalore 560064, India
[3]Max Planck Institute for Neurological Research, 50931 Köln, Germany
[4]DLR, Institute for Fluidmechanics, 37073 Göttingen, Germany

(Received 18 September 1997 and in revised form 9 October 1998)

We report here visualizations and quantitative measurements of scalar transport, under the influence of rotation, through permeable sediments with an overlying fluid layer. The experimental set-up considered here is a stationary cylinder containing a fluid-saturated porous medium up to its midheight, with supernatant water on top. A rotating lid generates, in the upper fluid region, a flow that partially percolates into the porous layer below. The velocity field in the fluid layer is obtained using particle image velocimetry (PIV). Further, dye transport from the sediment is studied using two different techniques. The first one is positron emission tomography (PET), a non-invasive method which allowed us to 'see' through the opaque solid matrix, and to obtain full three-dimensional pictures of dye transport through the sediment. The second one is digital photographic visualization from outside, and subsequent image processing in order to obtain the near-wall dye-washout depth. The experimental data suggest that the temporal evolution of washout depth for different sediments follows near-logarithmic behaviour. This finding is of importance for the *a priori* estimation of the transport of fluid and other solute substances in sandy aquatic sediments.

## 1. Introduction

Darcy's (1856) experiments on water flow through filter beds were the first attempts to quantify the flow phenomena in porous media, which resulted in the well-known 'Darcy's law'. Based on this law and its various extensions due to Dupuit (1863), Brinkman (1947) and Lapwood (1948) amongst others, a lot of experimental and theoretical studies on fluid flow and heat transfer through porous media have been inspired in the last decades relating to many diverse fields such as combustion, petroleum engineering, chemical and high-temperature fluid engineering, biotechnology and marine microbiology. Reviews by Scheidegger (1974), Greenkorn (1983), Kaviany (1991), Dullien (1992) and Nield & Bejan (1992) present clear pictures of the developments in this field.

Visualizations and measurements in porous media are difficult because of the existence of the solid opaque matrix and the limited optical and physical accessibility due to the obstructions provided by its random structure, situations which occur in nearly all natural permeable sediments (such as sand, clay etc.) and also in those that are of industrial significance, such as ceramic foams (Hall & Hiatt 1994, 1996). This difficulty is the main reason why in the bulk of the experimental studies in the past, 'constructed' or 'model' porous media have been preferred as the solid matrix.

For instance, Van der Merwe & Gauvin (1971) have used cubic packing of equal-sized spheres, Johnston & Dybbs (1975) a hexadiagonal close packing of Plexiglas spheres, whereas Tayal & Narayan (1990) constructed a porous medium by filling a horizontal rectangular Perspex cell with either glass beads of 1 mm diameter or 1–3 mm polystyrene particles.

With the development of laser Doppler anemometry (LDA) a new technique is now available for obtaining point measurements inside porous media. However, to apply this technique it is necessary to provide for minimal disturbance of the incident and the scattered laser light. This requires the use of transparent solid matrices (such as packings of glass beads), along with fluids whose refractive indices (at the laser wavelength) are closely matched to those of the solids. This match is accomplished usually by mixing two fluids (often mutually soluble silicone oils) whose specific properties must be found and parameterized in detailed experiments at constant temperature (see, for example, Saleh, Thovert & Adler 1992, and Rashidi & Dickenson 1996). Maintenance of constant temperature throughout the experiment is essential in order to avoid density and viscosity variations (Rashidi *et al.* 1996*a*). The variation of temperature in the measurement domain is also a source of problems while using optical techniques such as LDA and particle image velocimetry (PIV). When using LDA, the transverse refractive-index gradient due to temperature variations can shift the location of the measurement volume (Saleh *et al.* 1996). In order to avoid the difficulties in transmitting light through porous material while using the shadowgraph technique, Howle, Behringer & Georgiadis (1993, 1997) constructed their solid matrix such that the interfaces between the solid and the liquid are either parallel or perpendicular to the enclosing wall boundaries of the experimental apparatus. Many experiments have also been conducted using periodic arrangements such as lattice structures (e.g. Eidsath *et al.* 1983).

In some recent studies quantitative velocity measurements have been made in constructed porous media using non-invasive techniques such as particle image displacement velocimetry or PIDV (Saleh *et al.* 1992), LDA and PIV (Saleh *et al.* 1996), and particle tracking velocimetry or PTV (Peurrung, Rashidi & Kulp 1995). Shattuck *et al.* (1995, 1997) have studied the velocity distributions during the onset of convection in a porous medium by magnetic resonance imaging. Further visualizations at the pore level have been achieved by using a two-dimensional synthetic porous medium and digital image analysis (Soll, Celia & Wilson 1993), with glass micromodels, ultraviolet epifluorescent light and a dark-field microscope (Wan & Wilson 1994) and by a fluorescence imaging technique that can measure the velocity, concentration and the pore geometry (Rashidi *et al.* 1996*b*). However, instantaneous full three-dimensional visualizations inside the porous media have been difficult.

The development of computerized tomography (CT), a new radiological imaging technique, makes it possible to measure density and atomic composition inside opaque objects. The advantage of this method over the conventional X-ray radiography is that CT-scanners generate cross-sectional image slices through the object by revolving an X-ray tube around it and obtaining projections at different angles. Wellington & Vinegar (1987) used this technique for quantification of complex mineralogies, sand–shale ratios, $CO_2$ displacement in sediment cores, and viscous fingering.

A more recent and advanced tomographic imaging technique, applied usually in the field of nuclear medicine, is positron emission tomography (PET) which utilizes the characteristic radiation of positron-emitting nuclei. PET is an excellent non-invasive technique for three-dimensional imaging of the distribution of a radio-isotope inside an opaque system, and is used for *in vivo* imaging of physiological functions inside

the human brain. PET has been utilized in the past in the fields of petrophysics and reservoir engineering, allowing *in situ* monitoring of the physical processes. Van den Bergen *et al.* (1989) have used PET to examine the displacement of fluids in core-enhanced oil recovery and dehydration of water-in-oil emulsion.

Our present interest in investigating flow through porous media arises from related studies in the field of marine microbiology, where it has been found that advective flows driven by waves or tides, amongst others, can cause an exchange between the porewater and the overlying water at permeable sea-beds; this exchange, in turn, enhances the transport of nutrients, toxins and solute at the sediment–water interface (see, for example, Harrison, Musgrave & Reeburgh 1983; Huettel & Gust 1992). This process mentioned above is vital to the life-cycle of not only the organisms in the benthic layers, but also to marine life in general. Therefore, a great deal of experimental effort has been directed towards understanding the role of advective transport over the past years. The most often used tool for these investigations is the 'benthic chamber', usually of rectangular or circular cross-section, containing a certain depth of sediment along with supernatant water in which a recirculating flow is generated by means of a rotating disk. The porewater is first mixed with a tracer or dye and the advective exchange of fluid between the overlying water and the porewater is visualized at the end of the experiment by the rather cumbersome method of vertically cutting open the sediment core and observing the dye-washout patterns (see e.g. Huettel & Gust 1992). The 'dye-washout depth' in these experiments represents the depth of the region near the benthic chamber wall from where dye has been washed out (a more precise definition is given below); it has obvious relevance to depths inside the sea-bed within which exchange of many nutrients and solute takes place. In the experiments reported here, too, we study the variation of dye-washout depth for different sediments using a cylindrical benthic chamber with a rotating lid.

Among all the visualization and imaging techniques mentioned above, we find PET to be the most suitable for three-dimensional visualization of scalar transport in randomly packed opaque sandy sediments. Therefore, the first set of our experiments makes use of this technique. Besides this, a second set of experiments have been carried out using digital photographic visualization from outside, and subsequent image processing in order to obtain the long-time evolution of near-wall dye-washout depth for different types of sediments.

An outline of the paper is as follows. The experimental set-up and the general procedure are discussed in § 2. Technique and procedure specific respectively to the PIV and PET experiments, along with the results obtained, are presented in § 3 and § 4. The results from the digital photography method and comparison with PET are given in § 5. The concluding remarks § 6 includes a brief discussion of the results obtained. Finally, in the Appendix, we make estimates of the characteristic Reynolds number inside the sediment using dimensional arguments.

## 2. General experimental set-up and procedure

The experimental set-up used here is similar to a benthic chamber, and is shown schematically in figure 1. The system consists mainly of two parts: a stationary Plexiglas cylinder (carved out of a solid Plexiglas block in order to have a constant diameter through the whole length) of inner height $H = 15$ cm and inner radius $R = 5$ cm, and a rotating circular Plexiglas lid of radius 4.99 cm. A gap of 0.01 cm is left between the rotating lid and the cylinder wall in order to facilitate rotation. The lid is driven by a high-torque direct-current motor. The motor and the associated

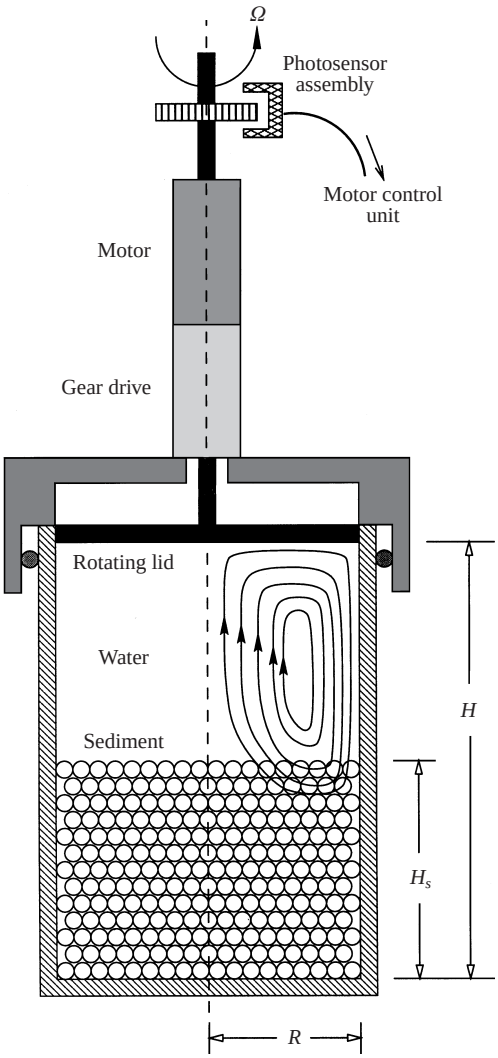


FIGURE 1. A sketch of the cylindrical apparatus or the 'benthic chamber'.

step-down gear-drive are mounted together inside a cylindrical casing of diameter 2 cm and height 8 cm. The speed of rotation of the motor can be changed easily from 1 to 12 revolutions per minute (r.p.m.) in steps of 1, using a solid-state motor-control unit that uses opto-electronic circuitry to maintain the angular speed of the disk within an accuracy of $\pm 0.001$ r.p.m. The photosensor assembly required for this purpose is mounted on top of the motor. In order to provide precise positioning of the rotating disk and better support for the motor and the gear-drive, the motor is mounted on a circular aluminium frame which sits snugly around the top of the Plexiglas cylinder. An O-ring made of silicone rubber is put between the cylinder and the frame.

To begin an experiment, the cylinder is first filled up to the height $H_s$ (which is the midheight in the present case or 7.5 cm from the bottom endwall) with a porous material. In order to achieve a flat sediment surface, the cylinder is softly tapped from the sides and gently shaken, and then a 'separator' (a circular disk of radius

| Sample | Diameter (mm) | Permeability, $\kappa$ ($m^2$) | Porosity, $\varepsilon$ |
|---|---|---|---|
| Glass beads | 2 | $2.8\times10^{-9} \pm 2\times10^{-11}$ | $0.39 \pm 0.01$ |
| Natural sand | 0.5–1 | $2.1\times10^{-10} \pm 3\times10^{-12}$ | $0.36 \pm 0.01$ |
| Natural sand | 1–2 | $6.8\times10^{-10} \pm 3\times10^{-12}$ | $0.38 \pm 0.01$ |
| Natural sand | 2–4 | $1.1\times10^{-9} \pm 5\times10^{-11}$ | $0.39 \pm 0.01$ |

TABLE 1. Different porous samples used in the experiments and their physical properties.

4.9 cm, with a long handle glued to it) is used to level the sediment surface. In the PIV experiments, the water filling the entire cylinder is pre-mixed with tracer particles. This procedure is, however, different for the PET experiments and the photographic visualizations where water mixed respectively with a radioactive material or black ink is used to fill the pores in sediment layer only. Excess dyed water, if any, is removed so that there is none of it above the top surface of the porous layer. Keeping the separator in place on top of the sediment layer, clear water is then added very slowly to fill up the cylinder. The separator serves two purposes: first, it prevents displacement of the solid matrix while filling clear water, and, second, it minimizes the pre-mixing of dyed water with clear water before the experiment has actually started. However, even if the separator is removed very carefully and slowly, a certain amount of pre-mixing cannot be avoided. We will address this issue later.

Successful experiments were carried out using two types of porous media, namely natural sands and spherical glass beads of different diameters and physical properties which are listed in table 1. The values of porosity and permeability of these samples were found by laboratory experiments. Porosity measurements were carried out using high-precision weighing equipments, and the permeabilities were measured in a manner similar to that described in Givler & Altobelli (1994). In order to obtain the range of values of porosity and permeability, for each sample five different measurements under similar conditions were made.

In the experiments reported here the disk angular velocity $\Omega$ is set to 12 r.p.m., which corresponds to a rotational Reynolds number of 3140 given by

$$Re = \Omega R^2/\nu$$

($\nu$ denotes the kinematic viscosity of water and is $1\times10^{-6}$ $m^2$ $s^{-1}$ at 20 °C). This is the highest Reynolds number achievable with the present apparatus; but as can be seen later, the rotation rate is adequate for obtaining reasonably large washout depths within times of the order of a few hours. Lower Reynolds number flows are not reported here since their effect on the dye distribution inside the sediment is found to be small. Note that the Reynolds number introduced above results from the characteristic flow parameters in the upper fluid layer, and that the flow problem is well-defined with this definition. However, in order to characterize the flow in the porous region, it has been a custom (Ward 1964) to introduce a 'superficial' Reynolds number based on the permeability of the porous medium $\kappa$ and the characteristic seepage or Darcy velocity $u_D$ (averaged fluid velocity over a volume element that contains both fluid and solid matrix) given by

$$Re_\kappa = \kappa^{1/2} u_D/\nu.$$

The pore-scale Reynolds number has also been presented in the literature (see Kaviani 1995; Nield & Bejan 1992) as a function of the diameter $d$ (associated with the porous

medium, i.e. the average grain or pore diameter) instead of permeability, and has been termed the 'particle' Reynolds number given by

$$Re_p = du_D/v.$$

Based on simple physical arguments and dimensional analysis that are detailed in the Appendix, we have made estimates of the characteristic Reynolds numbers associated with the flow inside the porous region. In the case of the 2 mm glass beads, for example, we estimate that $Re_\kappa \approx 0.01$ and $Re_p \approx 0.3$.

Other important parameters governing the flow are the aspect ratio of the upper fluid region

$$A = (H - H_s)/R$$

(= 1.5 in the present case), the porosity $\varepsilon$, the Darcy number

$$Da = \kappa/R^2$$

($\kappa$ is the specific permeability of the porous medium), and the Schmidt number

$$Sc = v/\sigma,$$

where $\sigma$ denotes the scalar diffusion coefficient.

## 3. Flow measurement in the fluid region via PIV

### 3.1. *Technique and set-up*

The flow in the fluid-only region was examined using particle image velocimetry (PIV) (Adrian 1991). To do this, the water filling the cylinder was seeded with 10 μm silver coated-glass spheres which may be considered as Lagrangian flow tracers. Local velocities in the flow are determined by using multiple time-delayed images of the particles.

Lighting consisted of a continuous light sheet created using a 1 W argon-ion laser. A schematic of the PIV set-up used is depicted in figure 2. The optical assembly employs a cylindrical lens, and a chopper disk. The cylindrical lens focused the beam to a height of approximately two times the height of the region of interest. The chopper disk (step-motor-driven and controlled by a high-precision signal generator) containing three slits rotates with an angular velocity that is adjusted to a light pulse frequency set equal to the repetition rate of the camera. This arrangement generates a light pulse length of 10 ms and a pulse separation time of $\Delta t = 40$ ms.

By placing the chopper disk at an angle, the beam passing through a glass plate (which covers one of the slits, see figure 2) is displaced sidewise, and two alternating parallel light sheets are generated. By this technique, referred to as 'dual-plane PIV', the velocity component normal to the light sheet planes can be obtained (Prasad & Adrian 1993). To observe the particle motion in the fluid-only region, a full-frame interline transfer CCD camera was used. Full-frame images of 752 × 582 pixels were recorded at a rate of 25 Hz. Also, as can be seen from the figure, the cylindrical container is placed into a rectangular one which is filled with water to eliminate optical distortions.

### 3.2. *Results*

PIV experiments were carried out in the cylinder containing 2 mm glass beads as solid matrix; the disk angular velocity $\Omega$ was set to 12 r.p.m. In order to give a clear picture of the flow in the fluid-only region, measurements in two different planes, namely

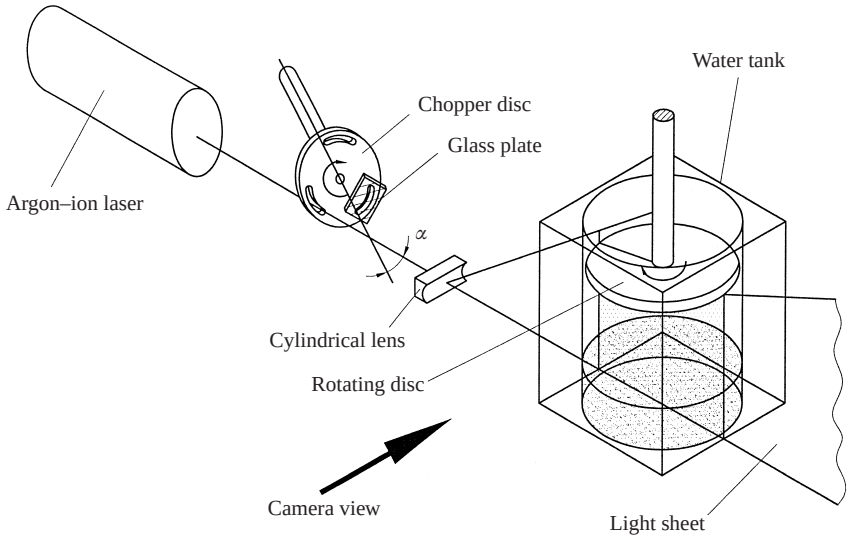


FIGURE 2. Sketch of the PIV optics arrangement in relation to the benthic chamber.

$(r, z)$ and $(r, \theta)$, were made ($r$ and $z$ are the radial and vertical directions and $\theta$ is the azimuthal angle). In the $(r, z)$-plane, the flow field dimensions are chosen such that the entire cross-section of the cylinder is captured. However, in the top view the field of view is limited to a 120° segment of a circle due to the existence of the cylindrical casing holding the gear-drive and the motor. Figure 3(*a*) shows an example of the velocity vector field in the $(r, z)$-plane after approximately 1.5 hour of disk rotation, obtained following post processing of the particle images. The corresponding velocity field in the $(r, \theta)$-plane is given in figure 3(*b*). As can be observed from the figures, the velocity fields suggest a nearly axisymmetric motion.

## 4. Positron emission tomography experiments

### 4.1. *Technique and set-up*

PET is a novel method for studying the distribution of substances labelled with positron-emitting isotopes. This technique is most often used in neurological research to obtain external quantitative measurements and visual representations of physiological quantities and metabolic parameters inside the human body. It combines the radioactive tracer technique and modern methods of generating overlap-free images with computer tomography. For a detailed description of this technique, the reader may refer to Eriksson, Dahlbom & Widén (1990). However, a short description of the basic principles involved is given here.

The positrons which are emitted from nuclei that have an excess of positive charge annihilate as they come into contact with electrons from the surrounding material, forming two photons. The photons are emitted with an energy of 511 keV each, colinearily in opposite directions. PET-detectors (which usually consist of bismuth germanate crystals linked to photo-multiplier tubes) detect both these photons at the same time and, thus, provide a kind of electronic collimation. Usually, the photon detectors are arranged in rings and, thereby, allow the detection of events that originate from a section through an object established by multiple pairs of detectors, called coincidence channels. Events are sorted into projections, where a projection is

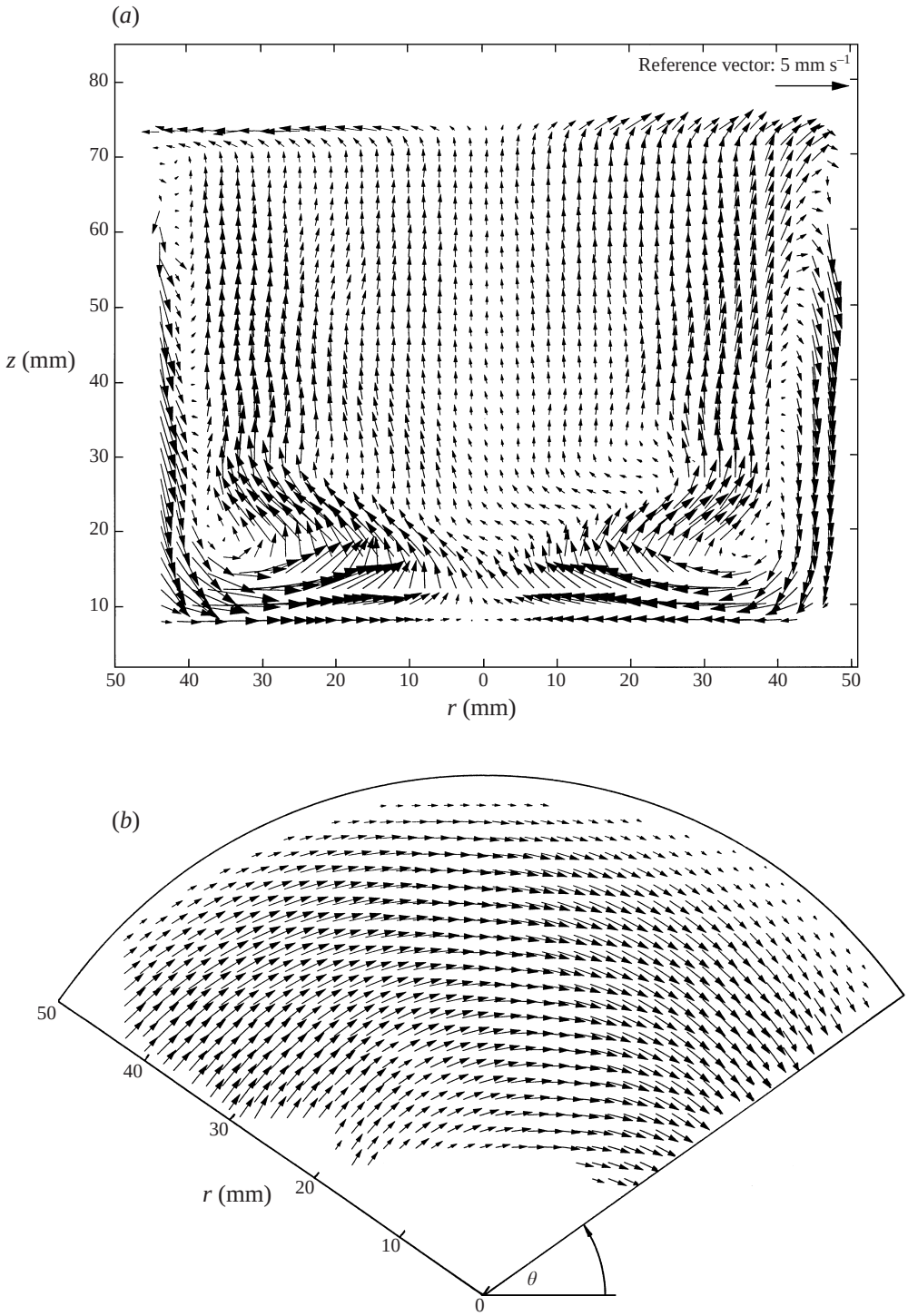


FIGURE 3. Example of the velocity field measurements in the fluid-only region in the benthic chamber: (*a*) entire $(r, z)$ (meridional) plane; (*b*) a 120° segment of the $(r, \phi)$ (equatorial) plane 1 cm above the permeable interface.

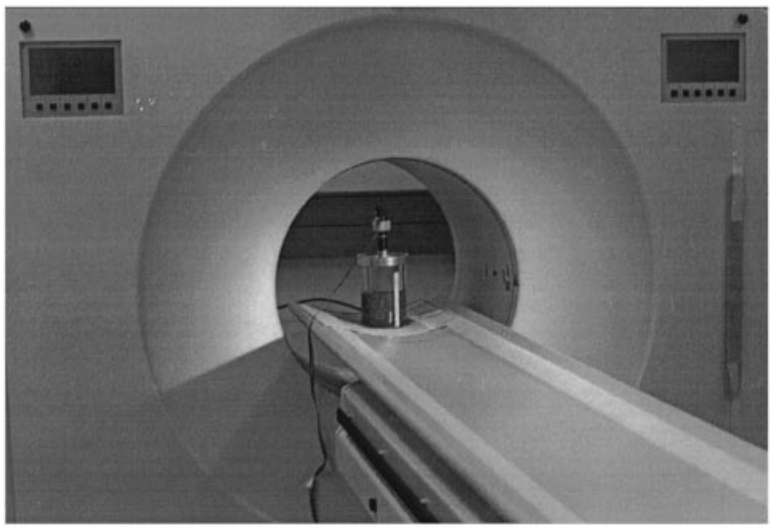

FIGURE 4. A photograph of the PET apparatus with the 'benthic chamber' in its scanning volume. The ring-shaped region is where the photon-detectors are located.

regarded as a number of neighbouring detector channels at different angles relative to the object's orientation. From the information stored in these projections the radio-isotope distribution within an object can be reconstructed. By means of fast reconstruction algorithms the projections are re-projected following a filtering that compensates for artefacts or errors which otherwise would occur. A part of the error originates from the fact that only a limited number of projections from different angles can be obtained, and also because of the finite size of the detectors that limits the spatial resolution within the projections.

Frequently, multiple detector planes are arranged such that the rings cover a cylindrical volume with a typical axial extent of 10–15 cm. Hence, the axial field of view is sufficiently large to span the entire cylindrical container in the present experiments (see figure 4, where a photograph of the PET system with the benthic chamber in its scanning volume is shown). The field of view of the tomograph used here (ECAT-EXACT, CTI-Siemens, Knoxville, USA) is scanned in 47 different parallel planes, 0.337 cm apart, along the plane of the detector rings. Each plane is made up of $128 \times 128$ pixels, 0.253 cm apart. While this resolution is certainly not very good, the present state of PET technology requires us to work within these limitations.

### 4.2. *Procedure*

Prior to the start of each experiment, a 'transmission scan' is made in order to calculate the corrections for photon attenuation of the experimental apparatus and the non-radioactive materials such as the sediment and water. A typical transmission scan is depicted in figures 5(*a*)–5(*c*), which show three different sections (two side views and a top view) through the body of the cylinder filled only with sediment (up to the midheight) and clear water (to the top) for this purpose; no radioactive tracer is added at this stage. Thus, the transmission scan provides the necessary calibration for calculating the true radioactivity at a later time. Note that the grey-scaled images show that the porous medium has higher attenuation than water.

Once the transmission scan has been made, the cylinder is re-filled up to $H_s$ with sediment and water mixed with fluordeoxy-glucose or F-18-FDG, which is the most

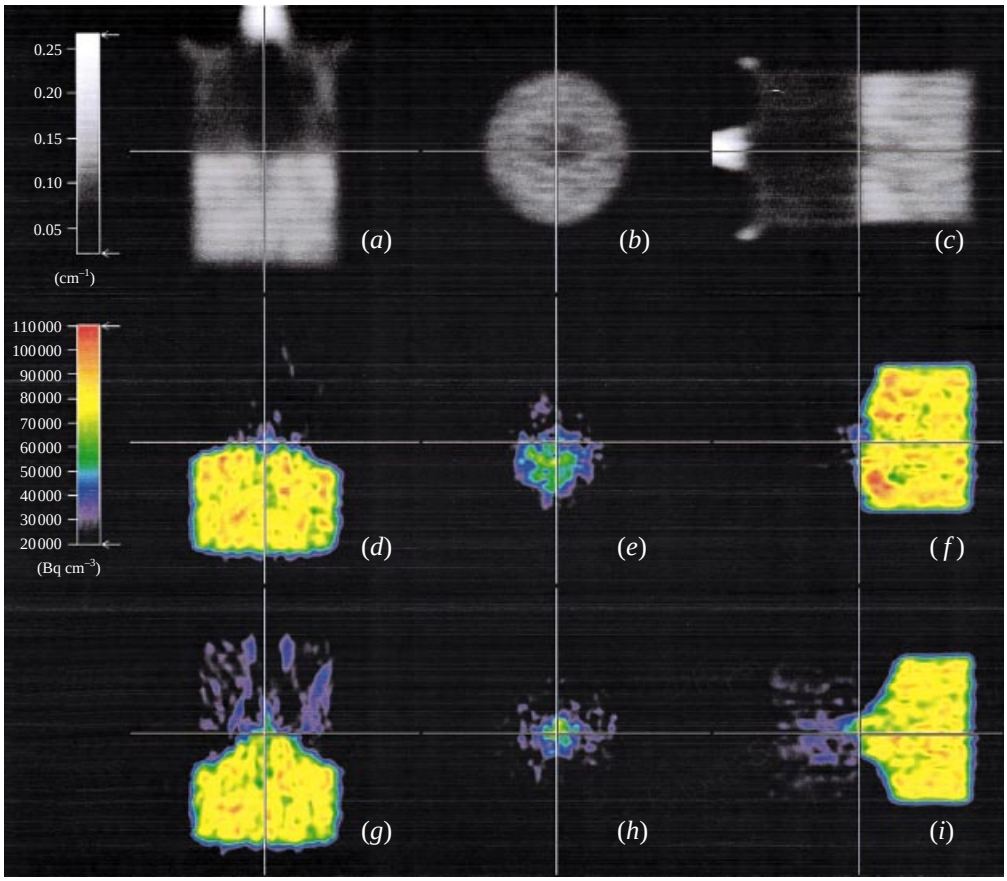


FIGURE 5. Typical sections through the cylinder obtained by the PET apparatus. The 'transmission scans' are shown in (*a–c*). The views in (*a*) and (*c*) are two vertical cross-sections passing through the axis of the cylinder, whereas (*b*) shows a transverse cross-section taken at the fluid–sediment interface. Different sections of the initial distribution of radioactivity are shown in (*d–f*), whereas the ones after 2 hours are in (*g–i*). The radioactivity is measured in Bq cm$^{-3}$, whereas the attenuation in the transmission scan is given in terms of cm$^{-1}$.

commonly used radioactive tracer in neurological medicine for estimating the amount of glucose in a patient's body. F-18-FDG has been chosen here in preference to other tracers such as O-15, C-11 and N-13 because of its reasonably long half-life of 109.8 minutes.

After placing the set-up in the field of view of the tomograph and setting the lid into rotation, scans of the dynamic flow and data acquisition start. Finally, using the attenuation corrections, the emission projection data can be reconstructed into emission images presented below.

### 4.3. *Results*

The results presented in this section are for a porous layer made up of randomly packed 2 mm diameter glass beads. For all the experiments, the data were acquired at intervals of 5 min over a maximum period of 3 h. Typical emission scans through the cylinder at the start of an experiment are shown in figure 5(*d*)–5(*f*), whereas those after 2 h are in figure 5(*g*)–5(*i*). Note that the transverse cross-sections (figure 5*b*, 5*e* and 5*h*) are obtained approximately at the fluid–sediment interface. In the colour images,

high radioactivity is coded as yellow and red, whereas low activity is in indigo and blue. The unavoidable pre-mixing we have alluded to before becomes obvious if one studies figure 5(*d*) and 5(*f*) carefully, which show definite depletion of radioactivity from regions near the water–sediment interface (shown by white horizontal lines in these figures) caused by the act of removing the separator. Note that all the data here are corrected for photon attenuation and also for natural radioactive decay. However, the data still suffer from the artefacts alluded to above, which show up as noise in the data, as high as 5% approximately. The other limitation of the present method is that it is only useful as long as the dye and the supernatant water are not completely mixed. In the present experiments, however, there is unmixed dye (radioactivity) inside the sediment even at the end of the experiment, and hence this limitation is not of serious concern.

Figure 5(*g*) and 5(*i*), at the end of the experiment, show depletion of radioactivity from the near-wall regions. This is related to the recirculating flow generated by the rotation of the disk. While the primary flow is along the azimuthal direction, the centrifugal pumping action generates a secondary flow which travels along the lid boundary layer (the Ekman layer) from the axis towards the outer wall, going down the wall forming the Stewartson layer, then moving along the sediment–water interface, and finally returning towards the top lid via the axis. Part of this recirculating flow percolates into the near-wall sediment layer and causes depletion of radioactivity there. These are the regions where significant exchanges of porewater and supernatant water take place. The schematic of the recirculating flow in the container is shown, representatively for the right half of the geometry, in figure 1.

In order to give a better picture of the washout process, a three-dimensional view is presented in figure 6, which depicts a single iso-surface of radioactivity intensity $\phi = 0.5$ at time $t = 2$ hours ($\phi$ here is normalized with respect to the maximum intensity at time $t = 0$). As can be seen from the figure, the distribution of radioactivity at this time is reasonably axisymmetric, except for small irregularities which are likely to be due to the artefacts mentioned above. The variation in colour intensity (grey scales) on the iso-surface is due to the solid modelling scheme of the graphics package used, and is retained here in order to give better representation of three-dimensionality.

The quasi-axisymmetry of the scalar distribution inside the porous medium in the present experiments makes it possible for us to average the data along the azimuthal direction. Such averaged pictures, with the dashed line denoting the fluid–sediment interface, are presented in figure 7(*a*)–7(*e*) at five different times. Each figure shows the section from the axis to the outer wall. As can be seen from figure 7(*a*), even at the initial instant there is depletion of radioactivity from both near the axis and the outer wall region due to the pre-mixing. The time evolution shows progressive depletion of radioactive tracer from the near-wall region, and a gradual increase in the upper fluid layer. Because of the presence of the aluminium frame that extends a little below the top lid from outside, there are errors in measurement of radioactivity in that region.

The values of porosity and permeability in the same sample may vary in general. Because the near-wall porous sample is usually not packed as efficiently as that in the interior, the value of $\varepsilon$ increases as one approaches the wall. Also the permeability is a function of the mechanism of permeation which is not the same in different directions, and is likely to be higher for flows along walls. From the results presented, it is difficult to conclude decisively whether this fact is of importance here. However, judging from the time-invariance of the near-wall radioactivity distribution (especially

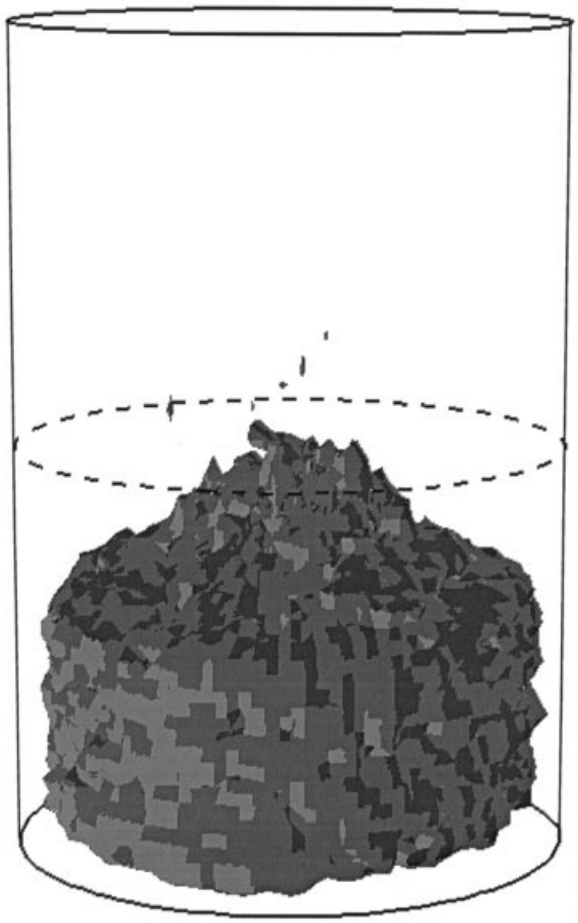

FIGURE 6. A typical three-dimensional iso-surface of the radioactivity distribution at time $t = 2$ hours; normalized intensity of $\phi = 0.5$. The outline of the cylinder is shown using solid lines, while the dashed line represents the fluid–sediment interface.

towards the bottom of the container) it is likely that this effect is not significant for this flow configuration.

From the above results, it is obvious that the PET technique provides a clear 'inside view' of the transport processes in an opaque porous medium using radioactive tracers. The importance of the data obtained using PET is twofold: first, to get clear three-dimensional views of scalar transport, and, second, to obtain a measure of the near-wall tracer-washout depth from the averaged pictures shown in figure 7. While the temporal evolution of this depth has been estimated from these data, we shall present it together with results of the dye-washout experiments in the next section.

## 5. Dye-washout measurement by digital photography

### 5.1. *Set-up and procedure*

To determine the evolution of the near-wall dye-washout depth over reasonably long periods of time, another set of experiments have been performed here. In these experiments, black ink (dye/water concentration 1/100) is used as the tracer, and

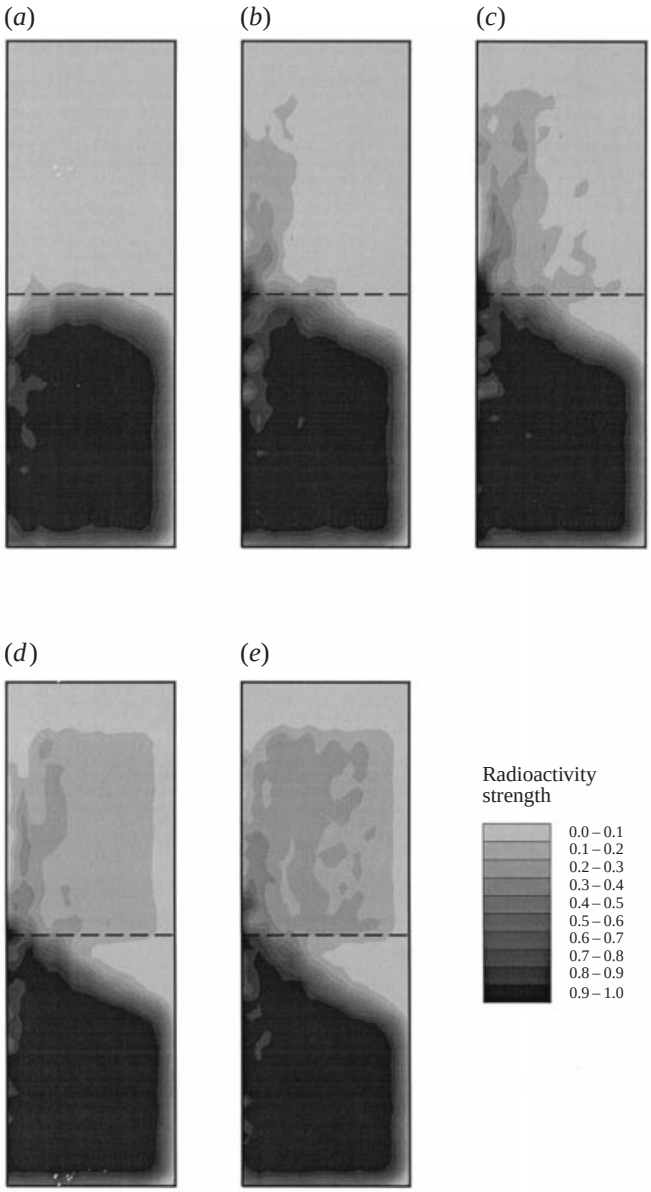


FIGURE 7. Azimuthally averaged radioactivity distributions inside the cylinder at different times: (*a*) $t = 0$, (*b*) $t = 30$, (*c*) $t = 60$, (*d*) $t = 90$, and (*e*) $t = 120$ min. Only the section from the axis to the outer wall is shown here. The dashed line represents the fluid–sediment interface.

the dye-washout depth is measured using digital photography and image processing techniques. The experimental set-up consists of the cylinder, a digital camera, and lights, placed inside an enclosure whose walls are made of black non-reflecting material in order to minimize the amount of diffused light. The lighting equipment consists of two 'cool' halogen lamps which are positioned to ensure that the side of the cylinder facing the camera receives as uniform a light as possible. This is achieved by analysing the pixel strengths in the digitized photographs for different light positions. The lights are switched on only during the measurements.

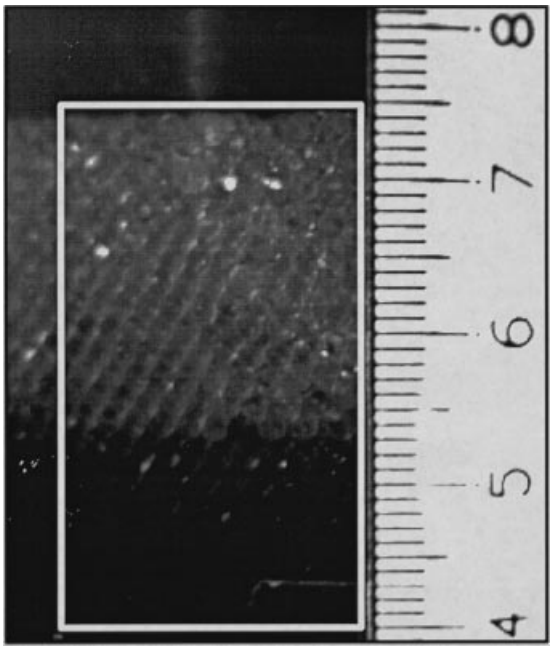


FIGURE 8. A typical 'cropped' image of the fluid–sediment interface obtained by digital photography. The 'control area' outlined in white is the region used for obtaining quantitative data. The fluid–sediment interface is near the 7.5 cm mark.

A solid-state CCD digital video camera (IndyCam, attached to a Silicon Graphics Indy workstation) is used in the black-and-white still photography mode to obtain pictures of the cylinder at different times during the experiment. The associated software which makes this photography possible is called 'capture', and is available with the workstation. A shutter speed of 1/100 s, and a 'gain' of 0.9 are used throughout the experiments. These settings were found to give the best contrast.

The camera is placed directly in front of the cylinder, at a distance of approximately 10 cm, and a height of 6 cm, with its line of focus passing through the cylinder axis. Because of the curvature of the container, the outer edges of the cylinder tend to get out of focus, and also suffer from considerable cylindrical distortions. Therefore, these regions were not considered for the present measurements. Figure 8 shows a typical 'cropped' image of a region around the fluid–sediment interface obtained by the camera. The image resolution is about 100 pixels per cm, which is considered sufficient for the present experiments, and is much higher than that obtained by PET. As can be seen from the figure, a metric scale is attached vertically along the cylinder wall so that actual physical distances can be ascertained from the pictures taken. The zero of the scale is positioned at the bottom endwall of the cylinder, and therefore, the sediment–fluid interface lies approximately at the 7.5 cm mark, as can be observed from the figure. It was decided to confine the measurements to a region much smaller than the full cylinder, namely to an area which is approximately 2 cm $\times$ 3.5 cm, spread equally over both sides of the plane passing through the axis of the cylinder and the camera lens having the fluid–sediment interface as the top boundary; it is outlined in white in figure 8. This region was chosen because within it: (i) the lighting intensity was found to be quite uniform, and (ii) the cylindrical error is minimum, indicated by a near-horizontal sediment–fluid interface. The line of dye washout also appears

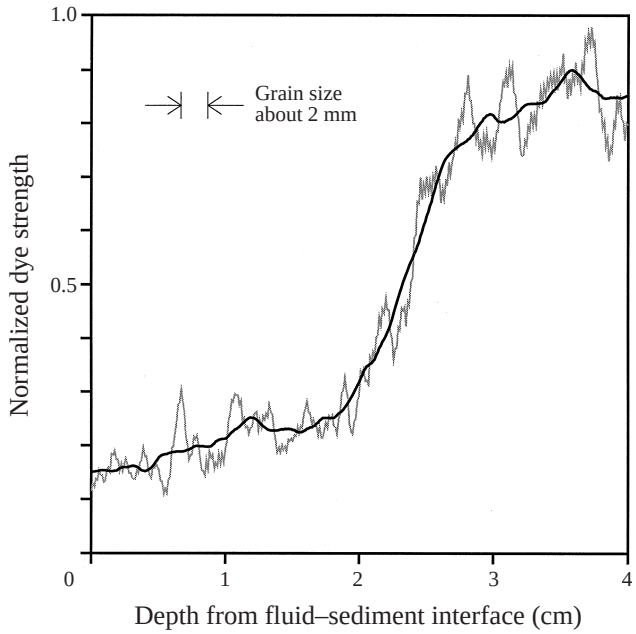


FIGURE 9. A typical (horizontally averaged) vertical distribution of normalized dye strength measured from the fluid–sediment interface, shown by the grey line, together with the corresponding smoothed line in black. The washout depth is defined as the depth at which $\phi = 0.5$.

nearly horizontal, signifying reasonable axisymmetry of the flow inside the porous medium. This section of the digitized picture then forms the main quantitative data for analysis by image processing techniques detailed below.

### 5.2. *Image processing*

The original images stored by the 'capture' program are image files in the Silicon Graphics RGB format, which are first converted into black-and-white or grey-scale images. Consequently, each pixel value falls in the range of 0 (pure black) to 255 (pure white) only. The pixel values within the 'control area' are read and scaled with respect to the maximum dye intensity at time $t = 0$, such that $\phi = 0$ represents a region with no dye, and $\phi = 1$ a region with maximum initial dye strength. The pixel values are then averaged along the horizontal direction; this process results in an average dye-strength distribution along the vertically downward direction below the interface. A typical representation of it is the highly fluctuating grey line given in figure 9. The oscillations in dye strength seen here are likely to be due to the presence of the sediment grains that cause unevenness in the dye strength which is also visible in figure 8. These fluctuations are removed here using the conventional 'moving-window averaging' technique. We have examined windows of width 8, 16, 32 and 64 pixels; the 32-pixel window was found to result in best smoothing without much disturbance to the original slope of the non-smooth line around the $\phi = 0.5$ region (see figure 9, smoothed line in black). This figure allowed a more precise definition for the washout depth ($\Delta_{0.5}$), which is the depth of the $\phi = 0.5$ point below the fluid–sediment interface. This measure appears to us to be a rational and objective one considering the sharp and almost constant gradient of dye strength around this point.

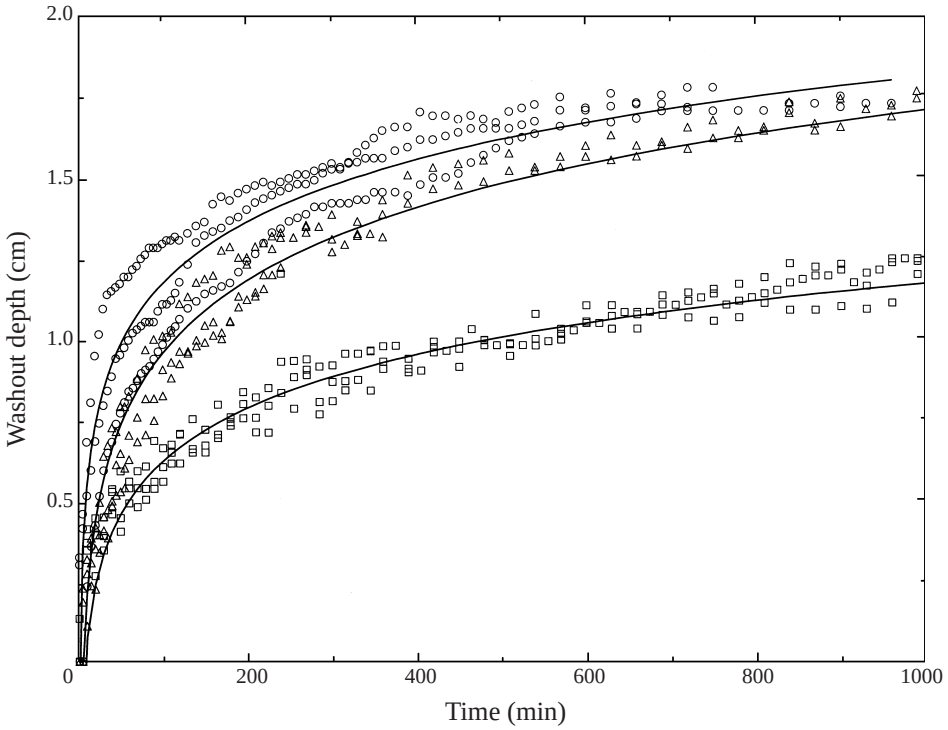


FIGURE 10. Evolution of the near-wall dye-washout depth for different sandy sediments, shown as a function of time. For each sand sample three different experiments were carried-out: □, 0.5–1 mm; △, 1–2 mm; ○, 2–4 mm diameter sand, respectively. The experimental data corresponding to each diameter are averaged, fitted using logarithmic functions and are shown by the solid lines.

### 5.3. *Results*

The experiments were carried out in a room with ambient temperature about $20\pm1$ °C and mainly with three different natural sands of diameters 0.5–1 mm, 1–2 mm and 2–4 mm. For each sediment, at least three different experimental runs were made, the longest amongst them lasting up to 20 h. The data were obtained every 5 min for the first 2 h, every 10 min for the next 2 h, every 15 min for the subsequent two hours, beyond which observations were made once every 30 min. In addition, short-time observations (up to 2 h) were made for the 2 mm spherical glass beads case, and the corresponding results will be compared with data from PET experiments later.

Figure 10 shows the temporal evolution of the near-wall dye-washout depth $\Delta_{0.5}$ for the three different sandy sediments used in the present experiments: 0.5–1 mm sand (□), 1–2 mm sand (△) and 2–4 mm sand (○) As can be seen from the figure, the washout depth increases with both time and grain size.

In order to simplify the analysis, all data belonging to the same grain size are reduced to a single curve using the averages of washout depths for each time $t$ and are plotted on the same figure after fitting; it can be easily seen that within the experimental time, the temporal evolution of the washout depths follow logarithmic distributions of the type

$$\Delta_{0.5} = a + b\ln(t)$$

which was found empirically. The values of the parameter pairs $a$ and $b$ differ for each grain size and are shown in table 2.

| Sample | Diameter (mm) | $a$ | $b$ | $C^2$ |
|---|---|---|---|---|
| Natural sand | 0.5–1 | −0.4525 | 0.2346 | 0.92 |
| Natural sand | 1–2 | −0.5193 | 0.3216 | 0.97 |
| Natural sand | 2–4 | −0.0806 | 0.2729 | 0.94 |

TABLE 2. Parameters used in the equation $\Delta_{0.5} = a + b\ln(t)$ to fit the experimental data empirically. The quantity $C^2$ in the last column is given by

$$C^2 = 1 - \sum_{i=1}^{n} \left[w_i(y_i - \hat{y}_i)/2\right] \Big/ \sum_{i=1}^{n} \left[w_i(y_i - \overline{y_i})/2\right] ,$$

and determines the goodness of fit. Note that, the closer the value of $C^2$ is to one, the better will be the statistical measure of the fit. The variables used in this relation have the following meaning: $n$ = number of data points, $w_i$ = weight, $y_i$ = $y$-data values, $\hat{y}_i$ = predicted $y$-values, and $\overline{y_i}$ = mean of $y$-values.

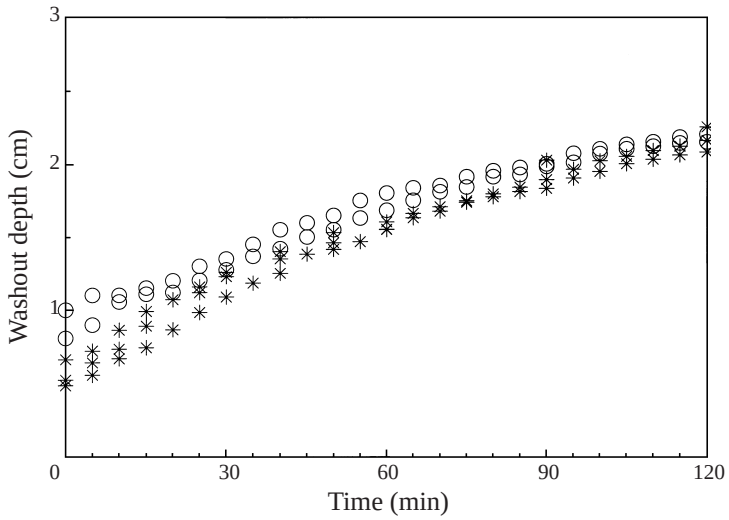


FIGURE 11. A comparison of the estimated near-wall dye-washout depths obtained from PET (○) and digital photography (★) All data are for 2 mm glass beads.

Finally, the results for near-wall washout depth from the PET experiments for 2 mm glass beads are presented in figure 11, together with those obtained using the digital photographic technique. From the PET data, washout depths are estimated by fitting a curve to the near-parabolic part of the $\phi = 0.5$ contour line below the fluid–sediment interface (from results such as those given in figure 7), and taking the depth at which that curve intersects the outer wall. As can be seen, there is reasonably good correspondence between the two sets of data.

## 6. Conclusion

The experimental study presented here explores a novel way of visualization of scalar transport inside opaque porous media, both natural and constructed, using PET. Full three-dimensional visualizations have been obtained at different times inside a 'benthic chamber' which contains a radioactivity saturated sediment with an initially clear fluid on top. Quantitative measures of dye-washout depth under the influence of rotation have been obtained by analysing the PET data.

PIV measurements of the velocity field in the fluid region have suggested nearly axisymmetric motion. Experiments have also been carried out to obtain measurements of dye-washout depth (as seen from outside) through the use of digital photography and image processing techniques. Three sandy sediments of different grain sizes, and consequently different porosity and permeability, have been studied for a constant rate of rotation of the disk. Logarithmic changes in the washout depth with time are observed in the present experiments. This finding is of importance for estimation of transport of solute in sandy aquatic sediments.

## Appendix. Estimation of the characteristic Reynolds number inside the porous region

As confirmed by the experiments reported in the present study, the nature of the flow above and below the interface is different: a large-scale advective flow above the interface and, in the first approximation, a Darcy flow below it given by the equation

$$u_D = -\kappa\mu^{-1}\nabla p$$

(Darcy 1856) in which $u_D$ is the characteristic 'Darcy' velocity inside the porous medium, $\kappa$ is the permeability, $\mu$ the viscosity of the fluid and $p$ is the pressure. The pressure gradient appearing therein originates from the flow in the fluid layer, caused by the disk centrifugal force and can be written

$$\nabla p \approx \rho(\Omega R)^2/(H - H_s),$$

where $\rho$ is the fluid density. Hence, a 'characteristic' velocity scale inside the sediment is approximately

$$u_D \approx \kappa(\Omega R)^2/(\nu(H - H_s)).$$

Replacing $u_D$ in the relations we gave for the Reynolds number inside the porous region (see § 2), we obtain $Re_\kappa = 0.0002$ and $Re_p = 0.012$ for the 0.5–1 mm sand, whereas for the 2–4 mm sand we obtain $Re_\kappa = 0.002$ and $Re_p = 0.233$.

The authors wish to thank B. B. Jørgensen, R. Narasimha and M. Kaviany for discussions on the subject, D. W. Heiss for his support and the referees for their constructive comments.

## REFERENCES

Adrian, R. J. 1991 Particle-imaging technique for experimental fluid mechanics. *Ann. Rev. Fluid Mech.* **23**, 261–304.

Brinkman, H. C. 1947 A calculation of the viscous force exerted by a flowing fluid on a dense swarm of particles. *Appl. Sci. Res.* A **1**, 27–34.

Darcy, H. P. G. 1856 *Les Fontanes Publiques de la Ville de Dijon.* Victor-Dalmont, Paris.

Dullien, F. A. L. 1992 *Porous Media Fluid Transport and Structure.* Academic Press.

Dupuit, A. J. E. J. 1863 *Études Théoriques et Pratiques sur le Mouvement des aux dans les Canaux Découverts et a Travers les Terrains Perméables.* Victor-Dalmont, Paris.

Eidsath, A., Carbonell, R. G., Whitaker, S. & Herman, L. R. 1983 Dispersion in pulsed systems: III. Comparison between theory and experiment for packed beds. *Chem. Engng Sci.* **38**, 1803–1816.

Eriksson, L., Dahlbom, M. & Widén, L. 1990 Positron emission tomography – a new technique for studies of the central nervous system. *J. Microscopy* **157**, 305–333.

Escudier, M. P. 1984 Observation of the flow produced in a cylindrical container by a rotating endwall. *Exps. Fluids* **2**, 189–196.

Givler, R. C. & Altobelli, S. A. 1994 A determination of the effective viscosity for the Brinkman–Forchheimer flow model. *J. Fluid Mech.* **258**, 355–370.

Greenkorn, R. A. 1983 *Flow Phenomenon in Porous Media.* Marcel Dekker.

Hall, M. J. & Hiatt, J. P. 1994 Exit flow from highly porous media. *Phys. Fluids* **6**, 469–479.

Hall, M. J. & Hiatt, J. P. 1996 Measurements of pore scale flows within and exiting ceramic foams. *Exps. Fluids* **20**, 433–440.

Harrison, W. D., Musgrave, D. & Reeburgh, W. S. 1983 A wave-induced transport process in marine sediments. *J. Geophys. Res.* **88**, 7617–7622.

Howle, L. E., Behringer, R. P. & Georgiadis, J. G. 1993 Visualization of convective fluid flow in a porous medium. *Nature* **362**, 230–232.

Howle, L. E., Behringer, R. P. & Georgiadis, J. G. 1997 Convection and flow in porous media. Part 2. Visualization by shadowgraph. *J. Fluid Mech.* **332**, 247–262.

Huettel, M. & Gust, G. 1992 Solute release mechanisms from confined sediment cores in stirred benthic chambers and flume flows. *Mar. Ecol. Prog. Ser.* **82**, 187–197.

Johnston, W. & Dybbs, A. 1975 Measurement of fluid velocity inside porous media with a laser anemometer. *Phys. Fluids* **18**, 913–914.

Kaviany, M. 1991 *Principles of Heat Transfer in Porous Media.* Springer.

Lapwood, E. R. 1948 Convection of a fluid in a porous medium. *Proc. Camb. Phil. Soc.* **44**, 508–521.

Nield, D. A. & Bejan, A. 1992 *Convection in Porous Media.* Springer.

Peurrung, L., Rashidi, M. & Kulp, T. 1995 Measurements of porous medium velocity fields and their volumetric averaging characteristics using particle tracking velocimetry. *Chem. Engng Sci.* **50**, 2243–2253.

Prasad, A. K. & Adrian, R. J. 1993 Stereoscopic particle image velocimetry applied to liquid flows. *Exps. Fluids* **15**, 49–60.

Rashidi, M. & Dickenson, E. 1996 Small scale flow process in aqueous heterogeneous porous media. *ASME Fluids Engineering Conference, San Diego, 7–11 July.*

Rashidi, M., Peurrung, L., Thompson, A. & Kulp, T. 1996*a* Experimental analysis of pore-scale flow and transport in porous media. *Adv. Water Resour.* **19**, 163–180.

Rashidi, M., Thompson, A., Kulp, T. & Peurrung, L. 1996*b* 3-D microscopic measurement and analysis of chemical flow and transport in porous media. *Trans. AMSE*: *J. Fluid Engng* **118**, 470–480.

Saleh, S., Thovert, J. F. & Adler, P. M. 1992 Measurement of two-dimensional velocity fields in porous media by particle image displacement velocimetry. *Exps. Fluids* **2**, 210–212.

Saleh, S., Thovert, J. F., Adler, P. M., Platten, J. K. & Bettignie, M. 1996 Measurement of thermally-induced convection in a model porous medium. *Appl. Sci. Res.* **55**, 245–259.

Scheidegger, A. E. 1974 *The Physics of Flow through Porous Media.* University of Toronto Press.

Shattuck, M. D., Behringer, R. P., Johnson, G. A. & Georgiadis, J. G. 1995 Onset and stability of convection in porous media: Visualization by magnetic resonance imaging. *Phys. Rev. Lett.* **75**, 1934–1937.

Shattuck, M. D., Behringer, R. P., Johnson, G. A. & Georgiadis, J. G. 1997 Convection and flow in porous media. Part 1. Visualization by magnetic resonance imaging. *J. Fluid Mech.* **332**, 215–245.

Soll, W. E., Celia, M. A. & Wilson, J. L. 1993 Micromodel studies of three-fluid porous media systems: Pore-scale processes relating to capillary pressure-saturation relationships. *Water Resources Res.* **29**, 2963–2974.

Tayal, P. & Narayan, K. A. 1990 Visualization of water and surfactant floods in oil-saturated porous media. *Exps. Fluids* **9**, 337–344.

Van den Bergen, E. A., Jonkers, G., Strijkmans, K. & Goethals, P. 1989 Industrial application of positron emmission computed tomography. *Nucl. Geophys.* **3**, 407–418.

Van der Merwe, D. F. & Gauvin, W. H. 1971 Velocity and turbulence measurements of air flow through a packed bed. *AIChE J.* **17**, 519–528.

Wan, J. & Wilson, J. L. 1994 Visualization of the role of gas–water interface on the fate and transport of colloids in porous media. *Water Resour. Res.* **30**, 11–23.

Ward, J. C. 1964 Turbulent flow in porous media. *J. Hydraul. Div. ASCE* **90**, 1–12.

Wellington, S. L. & Vinegar, H. J. 1987 X-ray computerized tomography. *J. Petrol. Tech.* **39**, 885–898.